

Rigid Impacts of Three-dimensional Rocking Structures

Péter László Várkonyi

Budapest University of Technology and Economics: Budapesti Muszaki es Gazdasagtudomanyi Egyetem

Tamás Ther (✉ ther@szt.bme.hu)

Budapest University of Technology and Economics: Budapesti Muszaki es Gazdasagtudomanyi Egyetem <https://orcid.org/0000-0001-7957-6843>

Márton Kocsis

Budapest University of Technology and Economics: Budapesti Muszaki es Gazdasagtudomanyi Egyetem

Research Article

Keywords: Rocking block, 3D rocking, Impact model

Posted Date: February 24th, 2021

DOI: <https://doi.org/10.21203/rs.3.rs-230986/v1>

License: © ⓘ This work is licensed under a Creative Commons Attribution 4.0 International License.
[Read Full License](#)

Version of Record: A version of this preprint was published at Nonlinear Dynamics on December 30th, 2021. See the published version at <https://doi.org/10.1007/s11071-021-06934-x>.

Rigid impacts of three-dimensional rocking structures

Péter L. Várkonyi¹ · Márton Kocsis¹ ·
Tamás Ther¹,

Received: date / Accepted: date

Abstract Studies of rocking motion aim to explain the remarkable earthquake resistance of rocking structures. State-of-the-art assessment methods are mostly based on planar models, despite ongoing efforts to understand the significance of three-dimensionality. Impacts are essential components of rocking motion. We present experimental measurements of free-rocking blocks, focusing on extreme sensitivity of impacts to geometric imperfections, unpredictability, and the emergence of three-dimensional motion via spontaneous symmetry breaking. These results inspire the development of new impact models of three dimensional facet and edge impacts of polyhedral objects. Our model is a natural generalization of existing planar models based on the seminal work of George W. Housner. Model parameters are estimated empirically for rectangular blocks. Finally, new perspectives in earthquake assessment of rocking structures are discussed.

Keywords Rocking block · 3D rocking · Impact model

Acknowledgements The authors thank Dr. Tamás Baranyai for his contribution to a preliminary version of the simulation code and for insights on singular points of the proposed impact map. This work has been supported by the National Research, Development and Innovation Office under grant 124002.

1 Introduction

Rocking is the typical response of many structures to dynamic loads such as earthquakes. Rocking structures include masonry columns, arches, walls [21, 27, 14, 7],

P.L. Várkonyi
Budapest University of Technology and Economics, Budapest, Hungary
E-mail: vpeter@mit.bme.hu

M. Kocsis
Budapest University of Technology and Economics, Budapest, Hungary

T. Ther
Budapest University of Technology and Economics, Budapest, Hungary
E-mail: ther.tamas@epk.bme.hu

innovative earthquake protection structures such as rocking shear-walls and frames [13, 36], and some tanks, machines or vehicles [16, 4, 20]. Understanding the non-smooth dynamics of rocking motion is essential to properly design and to assess the safety of these structures.

Rocking motion is an example of contact-induced hybrid multibody dynamics, where episodes of continuous motion are interrupted by short impacts. Rocking is inherently nonlinear, which prevents the use of the theory of linear vibrations [19]. Moreover the time history of rocking motion is notoriously unpredictable in many cases for two reasons [8, 33]. The lack of reliable and accurate impact models is a central problem of research concerning rocking motion. Modeling friction and transitions between stick and slip is another crucial question, even though the motion of many rocking structures (such as slender blocks) appears to be free of slip, and in such cases impact models are the only source of difficulty.

Impacts between hard objects have a very short duration. Accordingly, impact models used in the context of rigid body dynamics often take the mathematical form of an instantaneous mapping assigning a post-impact velocity to given pre-impact velocity state. Such discrete models are phenomenological descriptions of a complex, multi-scale physical process, and thus they are often unable to provide accurate predictions. In the case of straight impacts at a point contact, the *coefficient of restitution* is the standard phenomenological parameter, describing the motion in the normal direction. In the case of oblique frictional impacts, additional parameters are required to describe how the tangential and rotational motion of the colliding objects change during the impact process. Among others, a Coulomb-type coefficient of friction and the tangential coefficient of restitution are often used in this context. The parameters of impact maps are most often determined empirically or they are chosen a priori.

In the case of polyhedral rocking objects, impacts tend to occur in the presence of linear contact (Fig. 1.a,b) or surface contact (Fig. 1(c)). Both contact setups are geometrically degenerate in the sense that an arbitrarily small geometric imperfection may change the distribution of contact forces along the colliding edge or facet radically. For example the slightest concavity of the base of a rigid, planar rocking block results in the concentration of contact forces at the vertices (Fig. 2.a), whereas a slightly convex base may give rise to smooth rolling with the contact force sweeping along the whole edge (Fig. 2(b)) during the impact process. Obviously the outcome of an impact is *extremely sensitive* to such imperfections. This geometric sensitivity is the primary mechanism responsible for the unpredictability and irreproducibility of motion trajectories observed in physical experiments.

Housner's classical impact model for a planar rocking block [21] assumes that the impulse transmitted during a rocking impact occurs at the corner of the block, which is consistent with the assumption of a slightly concave base surface (Fig. 2.a). In contrast, physical experiments clearly indicate significant deviation from the predictions of Housner's model [30, 5, 26, 3, 31, 18, 34]. More recently, several authors proposed empirical model corrections [30, 5, 26, 3, 18], or a priori chosen geometric imperfections [34], to match the mean value of experimental measurements. Very recently, a few authors have proposed to consider the possibility of arbitrary geometric imperfections, in order to reproduce not only the mean, but also the observed variability of experimental results [10]. In the present paper, we

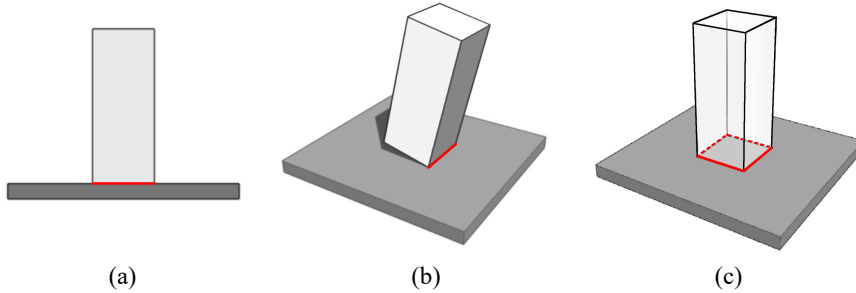


Fig. 1 Three types of rocking impacts: edge impact in a planar model (a), and in a 3-dimensional model (b); and facet impact in a 3D model (c).

revisit the problem of the planar rocking block, and present previous results using a unified approach in Section 2.

While the planar models uncover important aspects of rocking motion, real rocking motion is three dimensional, either because of out-of-plane excitation or as the result of spontaneously emerging out-of-plane motion even under planar initial motion and excitation. Relatively few works treat rocking as a 3D problem. The rocking motion of a rigid cylinder has been known for long time to be inherently three-dimensional [32]. Rocking cylindrical columns have been studied numerically by using rigid models [23, 35] as well as the Discrete Element Method [1]. Some experimental investigations focusing on the spatial rocking behaviour of ancient cylindrical columns have also been reported [29, 17]. It is notable however that cylindrical blocks behave differently than polyhedral objects as they typically “wobble” instead of undergoing impacts due to the lack of sharp vertices.

The first numerical model of 3D free rocking motion of a polyhedral block [24] focused on continuous motion, and did not propose an impact model. A similar analysis of an arbitrary rigid body with rectangular base by [38] proposed a natural 3D extension of Housner’s impact model by assuming that the impact impulse is concentrated at a vertex of the object. In addition the effect of slip was investigated in several papers [11, 12, 10].

Several authors including [38, 15] pointed out that the overturning of a 3D block can occur under excitations which are lower than those which overturn a corresponding 2D block. Hence 3D models are important for earthquake assessment. At the same time none of these works attempted to systematically investigate the set of possible outcomes of three-dimensional impacts and the role of geometric imperfections. In order to fill this gap, we introduce three impact parameters in the case of facet impacts, and two parameters for edge impacts, which capture all physically relevant outcomes of an impact without slip. Therby we obtain for the first time a *universal* 3D rigid impact model. The impact parameters of some free rocking blocks are determined via fitting simulated trajectories to experimental data. We use these results as well as basic physical laws to estimate the relevant ranges of model parameters.

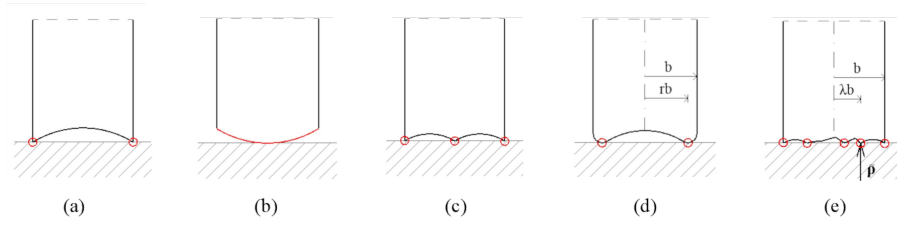


Fig. 2 Illustration of geometric imperfections and their effect on a planar rocking impact. A concave edge results in the impact model of Housner (a). A slightly convex edge (b) induces no energy loss. The model proposed by Ther and Kollár (c), and by Kallitzonis (d) are consistent with other imperfections. For an arbitrary imperfection, the possible outcomes of the impact can be parametrized by a single scalar λ representing the location of the resultant ρ of the impulsive forces (e).

The rest of the paper is organized as follows. In Section 2, we review the most common rigid, planar models of rocking impacts in a unified framework focusing on the case of a single monolithic block, and on the role of geometric imperfection. Then we present an experimental demonstration of transition from planar free rocking motion into three-dimensional rocking by a spontaneous symmetry breaking. This experiment confirms the crucial role of geometric imperfections. In Section 4, we develop the new, three dimensional model of rocking, which is highly analogous to planar models, but it can account for spontaneous symmetry-breaking. The experimental results are revisited in Section 5, and the parameters of the new impact model are fitted empirically. Section 6 concludes the work, and outlines future steps towards the successful application of spatial impact models in earthquake design.

2 A review of planar impact models

Consider a rigid, planar, rectangular object with mass m , and mass moment of inertia about the center of mass (COM) θ . Immediately before the impact, the block rolls around vertex V_b , until the base V_bV_a hits the ground. Let h and b denote the height of the COM of the block, and the half-length of V_bV_a , according to Fig. 3.a.

When the base of the block hits the ground, all points along V_bV_a come into contact simultaneously, and contact forces may emerge anywhere along V_bV_a . Housner's model assumes that

- H1: immediately before the impact, the block rotates about V_b
- H2: the rotational momentum of the block about the vertex V_a colliding to the ground is preserved
- H3: the vertex V_a stays in sticking contact with the ground after the impact

These assumptions determine uniquely the post-impact angular velocity of the block in terms of the pre-impact value as follows.

According to assumption H1, the velocity vector of the COM is $\mathbf{v}^- = \omega^- \cdot [h, -b]^T$. Similarly, assumption H3 implies that the post-impact COM velocity is

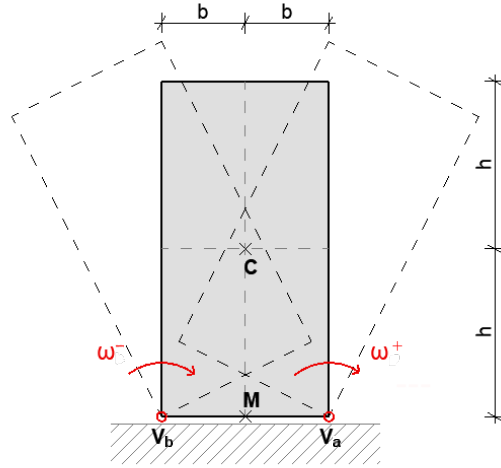


Fig. 3 Rocking impact of a free-standing block in two dimensions.

$\mathbf{v}^+ = \omega^+ \cdot [h, -b]^T$. The preservation of angular momentum about point V_a

$$\theta\omega^- + mh^2\omega^- - mb^2\omega^- = \theta\omega^+ + mh^2\omega^+ + mb^2\omega^+ \quad (1)$$

yields

$$\omega^+ = r \cdot \omega^- \quad (2)$$

where

$$r = r_{Housner} := \frac{\theta + mh^2 - mb^2}{\theta + mh^2 + mb^2} \quad (3)$$

The scalar r will be referred to as angular velocity reduction factor (AVRF).

If we introduce the following notions

- sticking impact: an impact where the impact point has 0 post-impact tangential velocity
- inelastic impact: an impact where the impact point has 0 post-impact normal velocity

then assumptions H2-H3 can be formulated in a more concise way as:

H4: a single, perfectly inelastic sticking impact occurs at the vertex V_a

While Housner's model does not include explicit assumptions about geometric imperfections, assumption H4 is consistent with certain geometric imperfections (Fig. 2.a) but inconsistent with others.

Many experimental works confirmed that the linear relationship (2) is a good approximation but the AVRF (3) derived using Housner's assumptions underestimates experimentally measured values [9]. To address this mismatch, several works

suggested improved models using either empirical modifications of the AVRF or modifications in Housner's initial assumptions [6, 26, 25]. In particular, Ther and Kollár [34] pointed out the crucial role of geometric imperfections. In order to improve model accuracy, they proposed an a priori infinitesimally small geometric imperfection (Fig. 2(c)), which implies that a rocking impact consists of a sequence of two elementary impacts at points M and V_a of Fig. 3. The smallness of the imperfection means that its effect on the physical properties (m, θ) of the block is negligible. Furthermore, the points V_b, M, V_a are almost collinear, which is captured by assumption

H5: The outcome a sequence of elementary impacts can be calculated as if they occurred immediately after one another in the nominal impact configuration of the perfect block.

In addition, H4 was replaced by a more general assumption

H4a: whenever a point of the imperfect surface hits the ground, a perfectly inelastic sticking impact occurs.

They showed that the corresponding AVRF

$$r = r_{TK} := \frac{\theta + mh^2}{\theta + mh^2 + mb^2} \quad (4)$$

closely matched the mean value of many physical experiments. Kalliontzis et al. [22] proposed using a reduced effective width of the base the length, which is consistent with assuming a geometric imperfection in the form of a concave section surrounded by two identical convex segments (Fig. 2(d)). The length ratios of the segments introduce a free parameter into the model and the corresponding value of r

$$r = r_{Kal} := \frac{\theta + mh^2 - m\nu^2 b^2}{\theta + mh^2 + m\nu^2 b^2} \quad (5)$$

can be anywhere in the interval $r \in (r_{Housner}, 1)$. Wittich and Hutchinson [37] examined a model with arbitrary geometric imperfection and demonstrated how the corresponding value of r can be determined under assumptions H1, H4a, H5.

Chatzis et al. [10] seems to be the first one to notice that if assumptions H1, H4a, H5 are combined with any type of infinitesimally small geometric imperfection, the emerging discrete or continuous distribution of linear momentum can be replaced by an instantaneous resultant momentum $[P_x, P_y]^T$ acting in a single point. The physically possible outcomes of the impact can be parametrized by a single scalar λ representing the position of the resultant impact force (Fig. 2(e)). Accordingly they proposed to use assumptions H1, H3 together with

H2a: the rotational momentum of the block about a specified internal impact point of the base given by the parameter λ is preserved

The AVRF now becomes

$$r = r_{Cha} := \frac{\theta + mh^2 - m\lambda b^2}{\theta + mh^2 + m\lambda b^2} \quad (6)$$

The straightforward assumptions of non-negative energy absorption implies $0 \leq \lambda$ whereas unilateral nature of contact forces imply $-1 \leq \lambda \leq 1$. Housner's

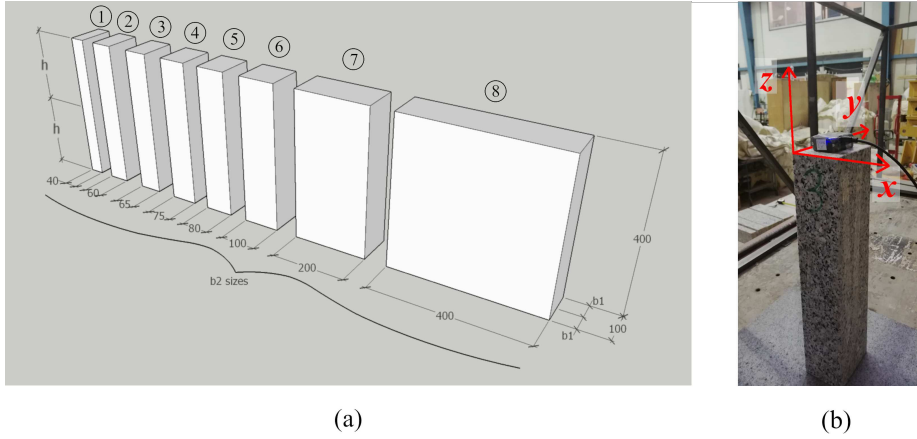


Fig. 4 The stone blocks used in the experiment (a), and the experimental setup with the coordinate system attached to the rocking block (b).

assumptions correspond to $\lambda = 1$, and smooth rolling on a slightly convex base (as in Fig. 2(b)) to $\lambda = 0$. We notice without proof that all values in the interval $\lambda \in (0, 1)$ can be realized by choosing an appropriate geometric imperfection. Thus, the resulting AVRF $r_{Cha}(\lambda)$ can take arbitrary values within the interval $(r_{Hou}, 1)$.

Importantly, the model of [10] is *universal*, i.e. it captures all possible post-impact states through a single scalar parameter λ despite the rich variety of possible geometric imperfections.

In Section 4, we develop a similar universal model of three-dimensional rocking impacts involving edge and surface contacts. Our contribution consists of a parametrization of possible outcomes along with theoretical limits of the model parameters.

3 Spontaneous emergence of out-of-plane motion in physical experiments

3.1 The experimental setup

The free rocking motion of 8 stone blocks (Fig. 4(a)) with identical heights h and width b_1 but different depths b_2 has been recorded with the aid of an X-IMU *inertial motion unit* device produced by *X-IO Technologies*. We use an orthogonal coordinate frame fixed to the rocking block (Fig. 4(b)) such that the x axis is parallel to the edge of length b_1 and the z axis points vertically up. During the experiments, each block shown in Fig. 4(a) was tilted in the xz plane and released five times. Then, each block was turned upside down, and the experiments were repeated. The two settings will be referred to as positions A and B. Fig. 5 shows time history data, which belong to the same granite block but the experiment was carried out in position A and B, respectively. Panel (a) shows components of the angular velocity, where nonzero values of ω_x or ω_z are both signs of spatial motion. Panel (b) depicts Euler angles φ_x , φ_y and φ_z representing the attitude of

the block using the *zyx convention*. (That is, a general rotation is the composition of three consecutive rotations about the local z, y, and x axes by angles φ_z , φ_y and φ_x .)

The X-IMU estimates time histories of the acceleration vector, angular velocity vector, attitude, and local magnetic field vector using on-board sensors including accelerometers, a triple-axis gyroscope, and magnetometers. Two operation modes are offered by the device. The Attitude Heading Reference System (AHRS) mode combines all sensor data including the magnetometer. We observed, that the big amount of steel equipment in the laboratory caused large systematic errors, and thus this mode could not be used. The Inertial Measurement Unit (IMU) mode excludes magnetometer data. This mode provides sufficiently accurate angular velocity estimations but large drift was observed in some of the attitude estimations (see Figure 5(b,e)). Throughout the experiment, we used IMU mode with 256Hz rate, and the drift of attitude data was compensated as described below (Figure 5(c,f)). The modified Euler angles were determined as follows:

- The local maximum points of $|\omega_y|$ in the angular velocity diagram were located numerically.
- These points mark the moment of an impact in which an edge of length b_1 is in contact with the ground. thus the φ_y , Euler angle should be zero
- A piecewise linear error function was added to the Euler angles to enforce 0 value of the appropriate components at the impact times.

The same correction steps were also repeated for the φ_x Euler angles.

3.2 Results of the experiment

Despite the xz plane being a plane of reflection symmetry, significant out-of-plane motion was observed in almost all cases (Fig. 5). In addition, large differences were observed between the A and B positions, whereas multiple trials in the same position yielded highly similar results. Both phenomena are the results of manufacturing imprecisions of the object, and our observations suggest that minor imperfections of the block strongly affect rocking motion.

In order to quantify these observations, two quantities were determined for every experimental trial:

- the *out-of-plane motion factor* (OPMF) is the ratio of the maximal absolute values of the Euler angles corresponding to out-of-plane and in-plane rotation $\Phi = \max_t |\varphi_x(t)| / \max_t |\varphi_y(t)|$ during the entire course of the rocking motion after the first impact.
- the AVRF was estimated based on 10 subsequent local maximum values of the corrected $|\varphi_y|$ inclination angle ($\varphi_{y,i}$; $i = 1, 2, \dots, 10$) of the block. First the vertical uplift of the COM at the maximal inclination angles was calculated as $u_i = h \sin \varphi_{y,i} - b_1(1 - \cos \varphi_{y,i})$. Then, an AVRF value corresponding to two adjacent maximum values was calculated as $r_{exp,i} = \sqrt{u_{i+1}/u_i}$. The final estimated AVRF r_{EXP} was the median of the 9 values corresponding to one single experimental trial.

The measured AVRF and OPMF values for different values of block depth (b_2) are depicted in Fig. 6. The out-of-plane motion factor was found to be as high

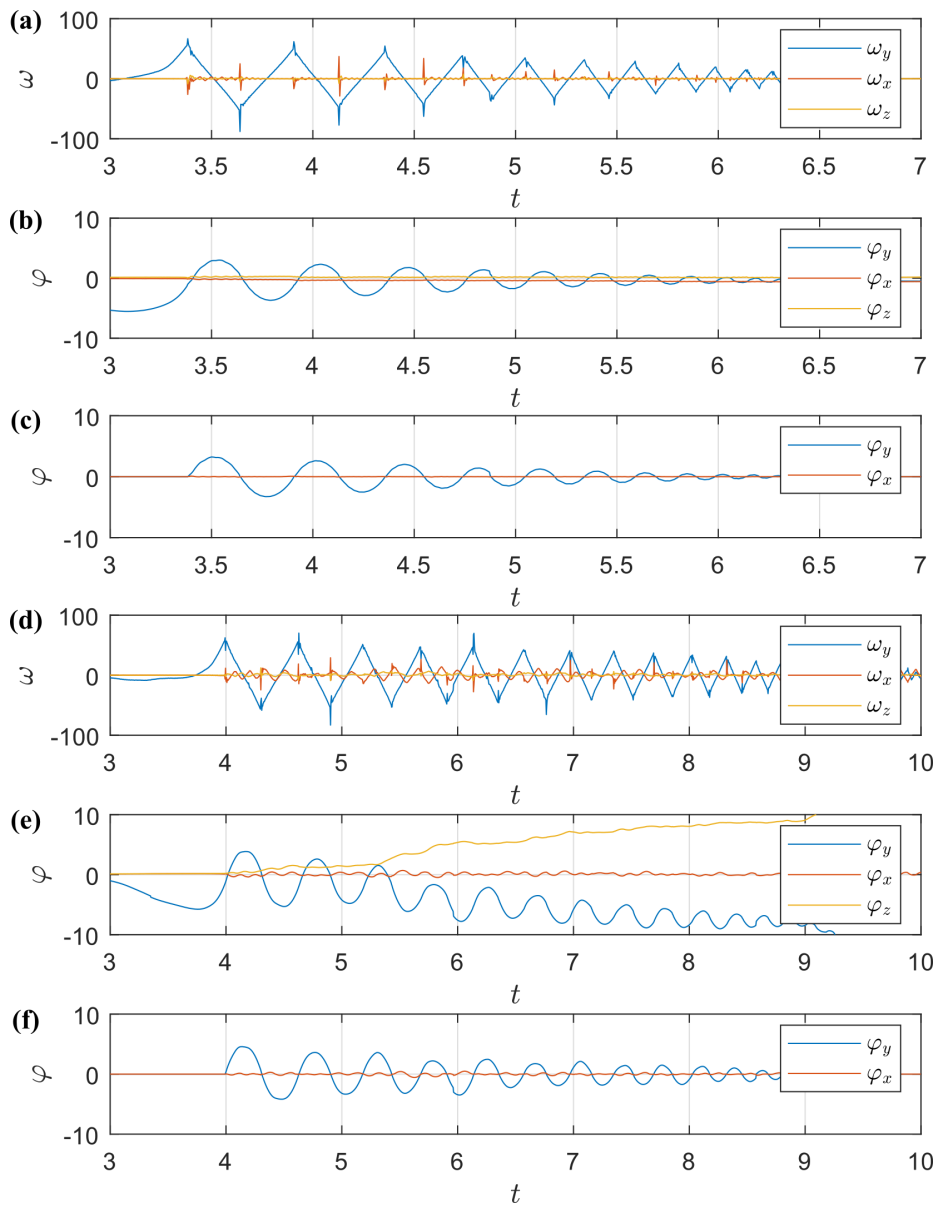


Fig. 5 Measured angular velocities (a,d), Euler angles (b,e), and corrected Euler angles (c,f) of the second block rocking in positions A (a-c) and B (d-f). Note large drift in (d).

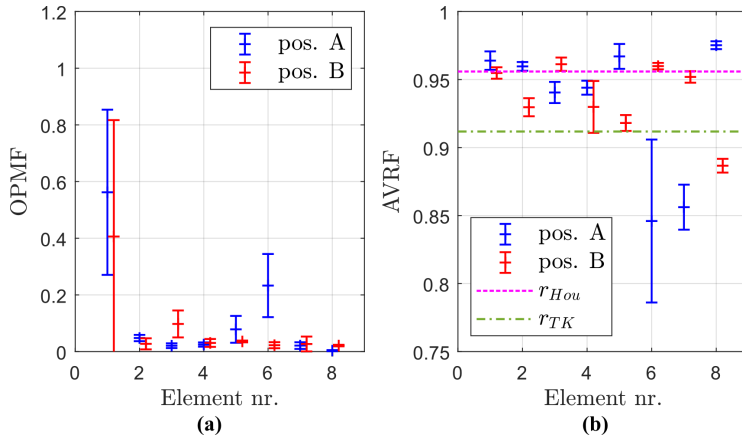


Fig. 6 Mean and standard deviation of measured out-of-plane motion factors (a) and angular velocity ratios (b) for each position (A or B) of the eight blocks.

as 0.5 for low values of b_2 , which is the result of spontaneous symmetry breaking induced by geometric imperfections. High dispersion of the AVRf data is likely also caused by imperfections, which can be explained by planar models. However the AVRf data also suggests that average values depend on b_2 , which cannot be explained by planar models. The amount of experimental data is insufficient to draw detailed conclusions about the role of b_2 however the presented results clearly indicate that such an effect exists. This is our motivation to present a new three dimensional impact model.

4 A new, three-dimensional impact model

4.1 The role of impacts during rocking motion

Three dimensional rocking motion of quasi-rigid, convex, polyhedral objects is a combination of continuous and discrete components. Contact-free motion is barely observed except for perhaps very small amplitude bouncing motion. Accordingly, most impact models use the assumption of perfect inelasticity. Slip may or may not be significant depending on contacting materials and geometry of the objects. Here we keep focusing on slip-free motion. With these restrictions, the possible contact modes of motion are surface contact (i(e). rest), edge contact (roll around the edge) and vertex contact (roll possibly with spin component). Transitions between these modes occur through impacts. More specifically, roll under vertex contact typically ends when all points along an adjacent edge of the block reach the ground simultaneously giving rise to an *edge impact*. The typical post-impact motion of slender rocking object is roll about the other endpoint of that edge. In a similar fashion, roll around an edge terminates when all points of the base facet reach the ground simultaneously, giving rise to a *facet impact*. Then, the typical post-impact mode is roll about a vertex of that facet. There are other possibilities just as a facet impact followed by roll about an edge or by

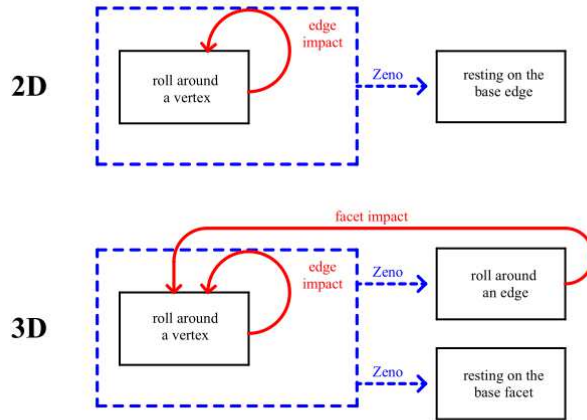


Fig. 7 Transitions during two and three dimensional rocking motion.

immediate immobilization. These are not typical for rocking motion and they are not considered by the current paper. In addition, vertex contact terminating in a surface impact is also possible but non-generic, so it is not discussed here.

It is worth noting that sustained edge or facet contact (rest) can not be created by any of the single impact transitions listed above. One of the special features of rocking motion is the possibility of infinite sequence of impacts in finite time intervals, which is often called *Zeno behaviour* [8, 2]. In planar models, a Zeno point occurs when motion stops. For three-dimensional models, a Zeno sequence of edge impacts may terminate in a state of rest or in a state of sustained edge contact (i(e). roll). This paper focuses on individual impacts, hence contact mode transitions through Zeno points are out of our scope. Figure 7 provides a schematic overview of the possible contact modes and generic transitions between them, including the Zeno behavior.

4.2 The resultant of the impact forces

Similarly to planar impacts, the outcome of a three-dimensional impact depends sensitively on geometric imperfections. It is again a reasonable assumption that the impact is instantaneous (in analogy to assumption H2 in Section 2), so the outcome of the impact is uniquely determined by the spatial distribution of impulsive forces along the edge or facet involved in the impact, and the exact time history of force during the impact process does not matter. Moreover, we can further simplify the description by considering the resultant of the impulsive forces in the spirit of Chatzis et al. [10].

There are however some differences between planar and spatial impacts. We have seen that an arbitrary distributed planar impulse is equivalent of a single resultant impulse, which has 3 free parameters (Fig. 8(a)). Two parameters are determined by the two kinematic constraints of rolling motion, and thus the possible outcomes of a planar impact can be parametrized by the remaining scalar parameter λ .

In contrast, the resultant of a spatially distributed three-dimensional impulse has 6 independent parameters and representation of the distributed impulse by an equivalent single resultant impulse (which has only 5 three parameters) is in general not possible. In the field of robotics, a distributed force is often represented by a 'wrench': a resultant force vector $\boldsymbol{\rho} = [\rho_x, \rho_y, \rho_z]$ along an appropriately chosen line of action (specified by two parameters) and an additional torque vector of magnitude τ parallel to $\boldsymbol{\rho}$. This representation is unique. Impulses can be represented in a completely analogous way by a resultant impulse and an angular impulse (Fig. 8(b)).

For convenience, we will use a slightly different representation of the distributed impulsive impact forces by using a 'modified wrench', which consists of the resultant impulse $\boldsymbol{\rho} = (\rho_x, \rho_y, \rho_z)$ and an additional *vertical* angular impulse vector of magnitude τ . The scalars x_R, y_R are used to specify the line of action of $\boldsymbol{\rho}$. This representation is also unique provided that $\rho_z \neq 0$.

Technically, the parameters of the modified wrench can be calculated in the case of facet impact as follows. Assume that the distributed impulse acts over a facet \mathcal{F} lying in the $x - y$ coordinate plane and it is given by the function $\mathbf{p}(x, y)$ with components $p_x(x, y), p_y(x, y), p_z(x, y)$. Then, the parameters of the modified wrench are calculated by surface integrals:

$$\boldsymbol{\rho} = \int_{\mathcal{F}} \mathbf{p}(x, y) dS \quad (7)$$

$$x_R = \rho_z^{-1} \int_{\mathcal{F}} x p_z(x, y) dS \quad (8)$$

$$y_R = -\rho_z^{-1} \int_{\mathcal{F}} y p_z(x, y) dS \quad (9)$$

$$\tau = \int_{\mathcal{F}} x p_y(x, y) - y p_x(x, y) dS \quad (10)$$

For edge impacts, \mathbf{p} is distributed along that edge, and analogous *linear* integrals are used to determine the resultant. If the distribution of the impulse is discrete, then summation can be used instead of integration.

The main advantage of the modified wrench representation is the fact that for arbitrary $p_z(x, y) \geq 0$, the possible locations of the point $R : (x_R, y_R, 0)$ are exactly the points of the facet \mathcal{F} according to (8)-(9). Similarly, for an edge impact, the possible locations of $R : (x_R, y_R, 0)$ are exactly the points of the edge involved in the impact. The latter will allow us later to use a single scalar parameter λ instead of x_R and y_R .

4.3 The impact map of edge impacts

Consider an edge impact of a rocking block with mass m and moment of inertia tensor Θ . Let $\mathbf{u}_x, \mathbf{u}_y, \mathbf{u}_z$ denote unit vectors along the coordinate axes. The pre-

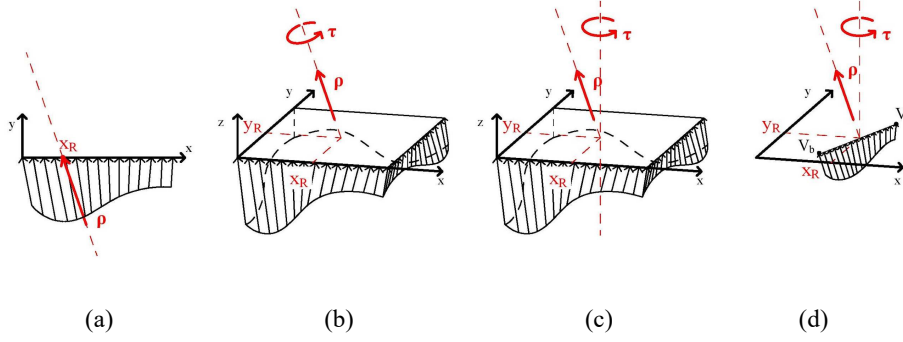


Fig. 8 Resultants of distributed impulses in 2 and 3 dimensions. A planar impulse (a) distributed along a line is equivalent of a single resultant impulse ρ , which can be represented by its components ρ_x, ρ_y and its location x_R . A three-dimensional impulse distributed along a surface can be represented by a resultant wrench (b) parametrized by the components ρ_x, ρ_y, ρ_z , and position x_R, y_R of the resultant ρ as well as by the magnitude of the torque τ . Alternatively, the same impulse can also be represented by a modified wrench consisting of a general impulse and a vertical angular momentum (c). An impulse distributed along a line section $V_b V_a$ can also be replaced by the modified wrench representation (d). In this case, the point $(x_R, y_R, 0)$ is a point of the section $V_b V_a$.

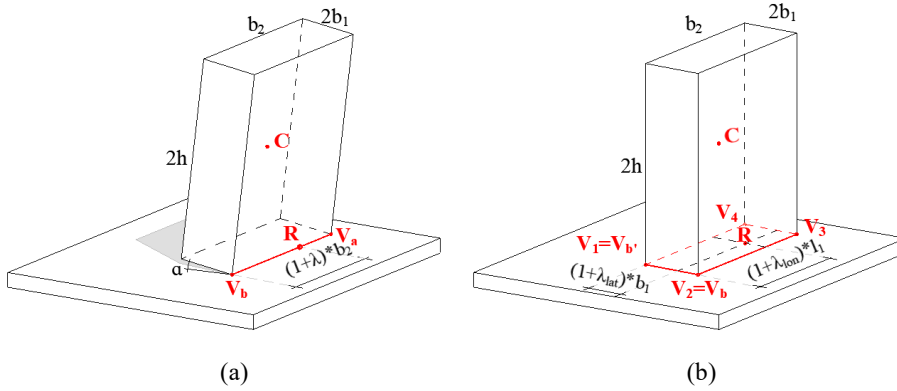


Fig. 9 Notation of edge impacts (a) and facet impacts (b) illustrated by a rectangular block of size $2b_1$ by $2b_2$ by h . In (b), we assumed that the index of the V_b vertex is $b = 2$.

and post-impact velocity of the center of mass, and angular velocity are $\mathbf{v}^-, \mathbf{v}^+, \omega^-, \omega^+$. V_b, V_a denote the two endpoints of the edge involved in the impact, with V_b being the point of contact before the impact, and V_a after. Let R denote the point where the modified wrench of the impact impulse intersects $V_b V_a$. The corresponding position vectors are $\mathbf{r}_b, \mathbf{r}_a, \mathbf{r}_R$, and \mathbf{r}_c is the position vector of the COM. As R is a point of the edge, one can introduce the scalar parameter λ such

that

$$\mathbf{r}_R = \frac{\mathbf{r}_a + \mathbf{r}_b}{2} + \lambda \frac{\mathbf{r}_a - \mathbf{r}_b}{2} \quad (11)$$

The impact impulse is represented by a set of 5 independent scalar parameters $(\rho_x, \rho_y, \rho_z, \lambda, \tau)$. The first three are determined by three kinematic constraints of rolling motion hence the possible outcomes of the impact have 2 free parameters: λ, τ .

The impact map $\boldsymbol{\omega}^- \rightarrow \boldsymbol{\omega}^+$ can be expressed as follows. The kinematic constraints of rolling motion immediately before and after the impact yield

$$\mathbf{v}^- = \boldsymbol{\omega}^- \times (\mathbf{r}_c - \mathbf{r}_b) \quad (12)$$

$$\mathbf{v}^+ = \boldsymbol{\omega}^+ \times (\mathbf{r}_c - \mathbf{r}_a) \quad (13)$$

The angular impulse momentum theorem applied to point R yields

$$(\mathbf{r}_c - \mathbf{r}_R) \times (m\mathbf{v}^+) + \boldsymbol{\Theta}\boldsymbol{\omega}^+ = (\mathbf{r}_c - \mathbf{r}_R) \times (m\mathbf{v}^-) + \boldsymbol{\Theta}\boldsymbol{\omega}^- + \tau\mathbf{u}_z \quad (14)$$

One can replace the cross products in (12)-(14) by matrix multiplication, using the matrix

$$\mathbf{R}_b = \begin{bmatrix} 0 & -\mathbf{u}_z^T(\mathbf{r}_b - \mathbf{r}_c) & \mathbf{u}_y^T(\mathbf{r}_b - \mathbf{r}_c) \\ \mathbf{u}_z^T(\mathbf{r}_b - \mathbf{r}_c) & 0 & -\mathbf{u}_x^T(\mathbf{r}_b - \mathbf{r}_c) \\ -\mathbf{u}_y^T(\mathbf{r}_b - \mathbf{r}_c) & \mathbf{u}_x^T(\mathbf{r}_b - \mathbf{r}_c) & 0 \end{bmatrix} \quad (15)$$

and two other matrices $\mathbf{R}_R, \mathbf{R}_a$ composed in the same way:

$$\mathbf{v}^- = \mathbf{R}_b\boldsymbol{\omega}^- \quad (16)$$

$$\mathbf{v}^+ = \mathbf{R}_a\boldsymbol{\omega}^+ \quad (17)$$

$$-\mathbf{R}_R(m\mathbf{v}^+) + \boldsymbol{\Theta}\boldsymbol{\omega}^+ = -\mathbf{R}_R(m\mathbf{v}^-) + \boldsymbol{\Theta}\boldsymbol{\omega}^- + \tau\mathbf{u}_z \quad (18)$$

Then $\boldsymbol{\omega}^+$ can be expressed as

$$\boldsymbol{\omega}^+ = (\boldsymbol{\Theta} - m\mathbf{R}_R\mathbf{R}_a)^{-1} \left[(\boldsymbol{\Theta} - m\mathbf{R}_R\mathbf{R}_b)\boldsymbol{\omega}^- + \tau\mathbf{u}_z \right] \quad (19)$$

As a last step, we use the identity $\mathbf{R}_R = (\mathbf{R}_a + \mathbf{R}_b)/2 + \lambda(\mathbf{R}_a - \mathbf{R}_b)/2$ (which follows from (11)) to obtain a closed form expression of the impact map in terms of known quantities and the two impact parameters λ and τ :

$$\begin{aligned} \boldsymbol{\omega}^+ = & \left(\boldsymbol{\Theta} - m \frac{\mathbf{R}_a + \mathbf{R}_b + \lambda(\mathbf{R}_a - \mathbf{R}_b)}{2} \mathbf{R}_a \right)^{-1} \dots \\ & \dots \cdot \left(\left(\boldsymbol{\Theta} - m \frac{\mathbf{R}_a + \mathbf{R}_b + \lambda(\mathbf{R}_a - \mathbf{R}_b)}{2} \mathbf{R}_b \right) \boldsymbol{\omega}^- + \tau\mathbf{u}_z \right) \end{aligned} \quad (20)$$

As we will see in Sec. 5, one can fix $\tau = 0$, and the remaining impact parameter λ still allows a reasonable fitting of simulated trajectories to experimental measurements.

4.4 The impact map of facet impacts

Let $V_i, i = 1, 2, \dots, n$ denote the vertices of the facet involved in the impact and \mathbf{r}_i the corresponding position vectors. Before a facet impact, the object rolls around an edge adjacent to that facet in general, which means two immobile vertices. (Recall that roll on a vertex followed by a facet impact is also possible but atypical, and this option is not considered now.) Let V_{b-1}, V_b ($b \in \{1, 2, \dots, n\}$) be the pre-impact axis of rotation. (The index $b - 1$ should be understood modulo n).

We assume that the object rolls around another vertex immediately after the impact. Let $V_a, a \in \{1, 2, 3, \dots, n\}$ denote a vertex immobile after the impact. Similarly to the case of an edge impact, the impact map has the form (19).

In this case \mathbf{r}_R cannot be expressed in terms of a single scalar parameter λ . Instead one can use the parameters x_R and y_R . Alternatively, if the facet is rectangular, then it is convenient to introduce two dimensionless parameters $\lambda_{lon}, \lambda_{lat}$ according to Fig. 9(b) such that

$$\mathbf{r}_R = \frac{\mathbf{r}_1 + \dots + \mathbf{r}_4}{4} + \frac{\mathbf{r}_{b+1} - \mathbf{r}_b}{2} \lambda_{lon} + \frac{\mathbf{r}_b - \mathbf{r}_{b-1}}{2} \lambda_{lat}. \quad (21)$$

Then, the impact map in terms of the impact parameters is given by (19), and (21) using the notation (15) for fixed values of a .

Importantly, the index a of the post-impact point of contact V_a cannot be chosen a priori in the case of a facet impact. The feasibility of all values of a can be tested one by one by evaluating the impact map, and by checking the requirements associated with unilateral contact:

$$\mathbf{u}_z^T \mathbf{v}^+ > \mathbf{u}_z^T \mathbf{v}^- \quad (22)$$

$$\mathbf{u}_z^T (\mathbf{v}^+ + \boldsymbol{\omega}^+ \times \mathbf{r}_i) \geq 0 \quad (23)$$

for $i = 1, 2, \dots, n$. The first formula reflects that unilateral contact forces should increase $\mathbf{u}_z^T \mathbf{v}$, and the second one means that none of the vertices penetrates into the ground after the impact.

Ideally this process should always provide a unique feasible solution, however this is not true in general. As illustration, we show numerical results of this process for a rectangular block of size 10 by 6 by 40 centimeter in Figure 11. The block rolls initially around edge $V_1 V_2$, and the facet $V_1 V_2 V_3 V_4$ hits the ground. The pre-impact angular velocity $\boldsymbol{\omega}^- = [0, -1, 0]^T$ is consistent with the kinematic constraints of rolling. The figure shows numerically identified regions of the impact parameters where the impact is followed by roll about vertex 3 and vertex 4 respectively. In addition, there are regions of the impact parameters where no feasible solution exists, and others where there are two solutions.

The observed non-existence of the solution means that there are non-trivial ranges of the impact parameters, which are *physically impossible*. In addition, non-uniqueness means that there are ranges of the parameter values where the chosen parametrization of impact is ambiguous.

In order to get rid of nonuniqueness and nonexistence, we will postulate that

$$\mathbf{u}_z^T \boldsymbol{\omega}^+ = 0, \quad (24)$$

i.e. there is no 'spinning' motion immediately after an impact. This assumption can be used to express τ . In the case of a homogenous cuboid block, we obtain

the trivial result $\tau = 0$. This assumption is plausible, as dry friction is likely to eliminate the spinning component of motion when a whole facet is in contact with the ground. As we will see, this assumption is also in agreement with experimental results. Finally, (24) guarantees a unique feasible solution as illustrated by Figure 11(a). A sketch of the proof of uniqueness is presented in the Appendix.

4.5 Theoretical limits of parameters of edge impacts

Similarly to planar impacts, the parameters λ , τ of edge impacts capture all possible outcomes, but it remains to find theoretical limits of these parameters. As we have seen, λ determines the position of the resultant ρ , which must belong to the segment $V_b V_a$. From this observation we obtain the limits

$$-1 \leq \lambda \leq 1 \quad (25)$$

Secondly, the impacts may not increase the kinetic energy of the rocking block. The kinetic energy of a rigid body rotating by angular velocity ω about a fixed point X can be calculated as $\frac{1}{2}\omega^T(\Theta + m\mathbf{R}_x^T\mathbf{R}_x)\omega$ where \mathbf{R}_x is the matrix composed from \mathbf{r}_x according to (15). Then we have

$$\begin{aligned} \Delta E := & \\ & \frac{1}{2}\omega^{+T} \left(\Theta + m\mathbf{R}_a^T\mathbf{R}_a \right) \omega^+ - \dots \\ & \dots - \frac{1}{2}\omega^{-T} \left(\Theta + m\mathbf{R}_b^T\mathbf{R}_b \right) \omega^- \\ & \leq 0. \end{aligned} \quad (26)$$

The region of the $\tau - \lambda$ parameter plane consistent with the last two constraints is always bounded, as λ is bounded by (25), and for each value of λ , ΔE is a quadratic function of τ with positive leading coefficient. It should also be noted, that for $\tau = 0$, (26) implies $\lambda \geq 0$ in analogy with previous findings about planar impacts. Figure 10 illustrates these bounds.

Another theoretical bound is provided by a singularity of the inverted matrix $\Theta - m\mathbf{R}_R\mathbf{R}_a$ in (19). We note without proof that such singularities do exist, but for slender blocks, they appear for large values of λ , which are irrelevant due to (25).

There is at least one more theoretical bound for edge impacts, which reflects the fact that the torque τ originates from frictional forces generated by tangential motion during the impact, thus it cannot be arbitrary. Finding the induced constraints of τ is beyond the scope of this work.

4.6 Theoretical limits of parameters of facet impacts

For facet impacts, bounds similar to those of edge impacts apply. First of all, the point R must be a point of the impacting facet. In the case of rectangular facets, this means

$$\begin{aligned} -1 &\leq \lambda_{lat} \leq 1 \\ -1 &\leq \lambda_{lon} \leq 1 \end{aligned} \quad (27)$$

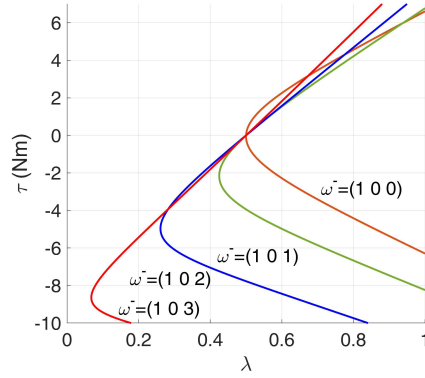


Fig. 10 Energy balance of an edge impact of a homogenous block of size 10 cm by 10 cm by 40 cm and total mass 1 kg at tilt angle of 5° for several pre-impact angular velocities. The regions of the parameter plane on the right sides of the curves result in reduction of the kinetic energy. The contour lines are not affected by multiplication of ω^- by a constant factor, or by adding an arbitrary y component to ω^- .

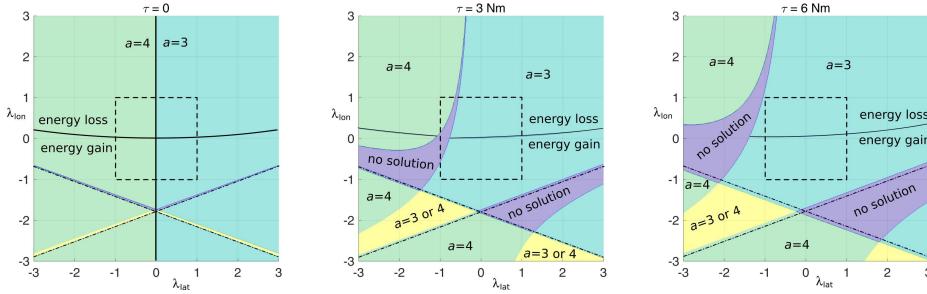


Fig. 11 Theoretical bounds of a facet impact of a block with $m = 1\text{kg}$, $b_1 = 5\text{cm}$; $b_2 = 3\text{cm}$; $h = 20\text{cm}$. Pre-impact angular velocity is $\omega^- = [0, -1, 0]$, which corresponds to roll around edge $V_1 V_2$. Each panel shows results for fixed values of τ . Background colors show the index a of the vertex in contact with the ground after the impact. Regions with no valid solution and two valid solutions also exist. Dash-dotted lines depict the singularity of (19). Dashed rectangles depict the region (27); the energy bound (26) is satisfied in the region above the continuous curves.

The energy bound (26) (solid curves in Fig. 11) as well as the singularity of (19) (dash-dotted curves in Fig. 11) are also applicable to facet impacts. Again, we note without proof that the singularity appears for irrelevant ranges of $(\lambda_{lat}, \lambda_{lon})$ provided that the block under investigation is slender. In addition, there are bounds of τ similarly to edge impacts that we do not investigate in this paper.

A new type of theoretical bound for facet impacts is given by those regions of the model parameters, where no feasible solution exists (Fig. 11). As it has been pointed out, we avoid the potential nonexistence of solution by assuming (24).

5 Empirical fitting of impact parameters

5.1 Methods

We now revisit the experimental tests introduced in Section 2. The motion always starts with the following four episodes:

1. initial roll around edge V_1V_2
2. facet impact
3. episodes of roll about vertex V_3 and V_4 each of which is terminated by an edge impact at edge V_3V_4
4. an edge impact when either V_1 or V_2 reaches the ground

In order to reproduce the observed motion numerically, we developed a custom-made code in MatLab environment, which simulates roll motion on any vertex or edge as dictated by the Newton-Euler equations of rigid body motion. This was complemented with an event detection algorithm to detect the impact times and with a numerical implementation of the impact maps introduced in Section 3. The code follows the logical structure of Fig. 7 except that detection of Zeno points has not been implemented. This code is able to simulate rocking motion of a block until the first Zeno point, if the physical properties of the block (size, mass, moment of inertia), the initial time of release t_0 , initial tilt angle α and the parameters of edge impacts (λ, τ) and of facet impacts ($\lambda_{lat}, \lambda_{lon}, \tau$) are specified.

The aim of this code is to find optimal values of the initial conditions and impact parameters, matching the experimentally measured trajectories. To that end we introduce the error function

$$\epsilon(t_0, \alpha, \dots) = (t_{end} - t_0)^{-1} \int_{t_0}^{t_{end}} |\omega_m(t) - \omega_s(t, t_0, \alpha, \dots)| dt \quad (28)$$

where t_{end} is the time when the sequence of episodes listed above ends. ω_m , and ω_s are measured and simulated angular velocity functions, and ω_s depends on the initial conditions and model parameters introduced above. In order to reduce the number of unknown parameters, we fix $\tau = 0$ both for edge and for facet impacts. In addition, we assume that each of the $\lambda, \lambda_{lat}, \lambda_{lon}$ impact parameters take constant values along an individual rocking test. The unknown initial conditions (t_0, α) and the model parameters $\lambda, \lambda_{lat}, \lambda_{lon}$ have been determined by semi-automated numerical minimization of the error function ϵ : a rough fitting was first obtained by trial-and-error, the results of which was used as initial guess in the *fminsearch* numerical optimization algorithm of MatLab software [28]. An example of trajectory fitting is depicted in Fig. 12 and the optimum values are summarized in Fig. 13 for blocks 1 to 6 and for both position (A or B). The fitting was omitted for blocks 7 and 8, which tended to produce Zeno behavior. In the next two subsections, two important observations about these results are presented.

5.2 The reason of noisiness

The first observation from Fig. 13 is the presence of large noise in the parameter values. This is partly caused by noisy experimental data. For example, impacts

often cause rapid oscillations in measured angular velocity values (see Fig. 12), which is likely an artifact caused by mechanical vibration of the gyroscopes. However large noise also reflects the sensitivity of impacts to geometric imperfections, which may even change between subsequent impacts as a result of small grains under the rocking block. The observed noise is thus more than just a weakness of our approach. It indicates that impact parameters should be treated as uncertain parameters during the analysis of rocking motion. For example earthquake response analysis should verify the safety of a rocking system for a whole range of impact parameter values rather than for single values of those parameters.

5.3 The relevance of theoretical bounds

A closer look at the fitted λ_{lon} parameter values reveals that they are in the range $(0, 1.5)$. This is consistent with the bound (26), however the limit (25) is often violated by λ values exceeding 1. Large λ means that more energy is absorbed during the impact, and we believe that the unexpectedly large values were primarily caused by the fact that a real block loses energy during roll motion due to rolling friction, however our model omits this option. The lack of energy absorption during roll is compensated by higher λ_{lon} values during impacts. The same explanation applies to the unexpectedly high λ parameter values of edge impacts.

The fitted λ_{lat} values are in the interval $(-5, 5)$, which is far beyond the limit (27). This is partially explained as follows: one of the widely established assumptions in the literature of rocking motion is that of perfectly inelastic impacts (see assumption H4 in Sec. 2). Clearly, this assumption is merely a phenomenological description of the impact process. In reality, a light impact of a stone block on a steel surface generates an almost perfectly elastic impact, followed by bouncing motion. In the case of slender blocks, the bouncing motion has very small amplitude, and short duration, hence the assumption of inelasticity yields seemingly accurate description of the macroscopic motion. However this assumption introduces large error when our aim is to estimate the emerging out-of-plane angular velocity. To illustrate this phenomenon, imagine a facet impact, in which the resultant of the impact momentum acts near vertex V_3 (see Fig. 11). Then the model predicts roll about vertex V_4 after the impact. If the impact is not ideally inelastic, then more vertical momentum is transferred to the block than the momentum predicted by the inelastic model. The surplus momentum causes the block to jump in the air, and to undergo bouncing on V_4 instead of smooth roll. Moreover the surplus momentum at V_3 during the impact is compensated by less momentum transferred to V_4 after the impact than the momentum generated by pure rolling motion during the same time interval. The surplus momentum emerging at V_3 instead of V_4 amplifies the out-of-plane angular velocity of the block after the facet impact. This is captured by $|\lambda_{lat}|$ values exceeding 1.

Hence, our second important observation is that the optimal fit of impact parameters to experimental results may yield parameter values contradicting previously found theoretical limits. Rather than being an error, these unexpected values indicate that the model can successfully capture the effect of neglected phenomena such as small-amplitude jumping motion and rolling friction. These results suggest that empirically determined ranges of impact parameters should be used instead of the theoretical limits derived above. The amount of available

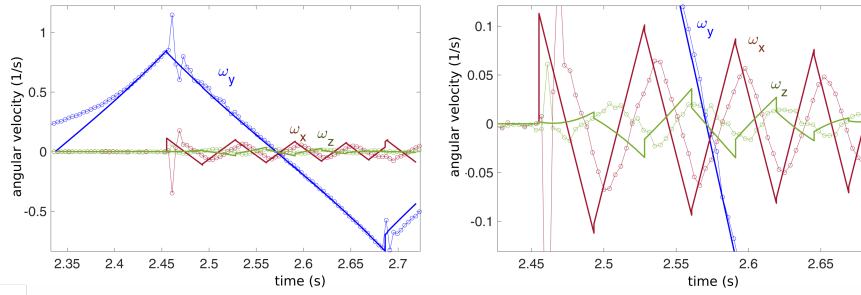


Fig. 12 Left: Circles show measured angular velocities of block 4 in a free rocking test. Solid line shows simulated trajectories with optimized parameters: $t_0 = 2.33\text{s}$; $\alpha = 0.197\text{rad}$; $\lambda = 2.185$; $\lambda_{lat} = -2.032$; $\lambda_{lon} = 0.197$. Right: magnified detail of the previous diagrams. Note that each impact induces an instantaneous jump in the angular velocity, however in some cases the jump is too small to be visible.

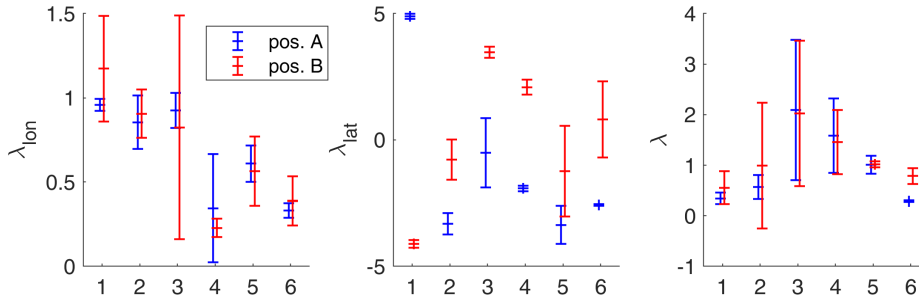


Fig. 13 Numerically fitted impact parameters for the A and B positions of blocks 1 to 6.

experimental results is insufficient to accurately determine the relevant ranges of parameter values, which is left for future work.

6 Conclusions

The remarkable earthquake resistance of rocking structures inspires ongoing efforts to understand the characteristic features of rocking. The challenges of the analysis include strong nonlinearity (even at small amplitudes), hybrid dynamics (sudden impacts and continuous motion), and geometric sensitivity (associated with edge and facet impacts). Models used for the analysis of rocking motion often use various simplifying assumptions, such as rigidity, inelastic impacts, slip-free motion, and planar motion.

Our work was inspired by the well-known observation that free rocking blocks tend to transition from planar motion to spatial rocking via spontaneous symmetry breaking. This is caused by microscopic geometric imperfections of the block, which have macroscopic effect on the motion due to the extreme geometric sensitivity of edge and facet impacts of quasi-rigid objects. This phenomenon cannot be

explained by currently available models, and calls for a new modeling approach, which is three dimensional and non-deterministic. As a first step towards such a model, we proposed a new *universal*, three-dimensional impact model, which can be used in the context of rigid body dynamics. *Universality* means that all reasonable outcomes of the impact are described by a small set of impact parameters. Our new model is a natural extension of the planar impact model [10], which uses one single impact parameter.

The parameters of the new impact model have been fitted to some free-rocking experiments. The results show that the parameters are quite unpredictable, which is not surprising as they capture the effect of unknown geometric imperfections. We made initial steps towards identifying possible values of the impact parameters, however more experimental data will be required to accurately identify their relevant ranges and probability distributions.

The long-term goal of our research effort is to improve current methods of assessing the earthquake resistance of rocking structures. We foresee that the inherently three-dimensional nature of rocking motion affects the ability of a structure to resist earthquakes without overturning. Moreover, the unpredictability of impact parameters suggests that parametric studies may be necessary to assess the safety of a structure.

Declarations

The authors declare that they have no conflict of interest. Experimental data and the code generated for the impact model are available from the corresponding author by request. This work has been supported by the National Research, Development and Innovation Office under grant 124002.

A Uniqueness of the facet impact map

It was demonstrated by numerical simulation (Fig. 11) that for some values of the impact parameters, the facet impact map may have no feasible solution or multiple feasible solutions. However Fig. 11(a) strongly suggests that there is always one unique solution under (24) (or equivalently $\tau = 0$). Here we sketch the proof of uniqueness in this case.

For fixed values of the impact parameters λ_{lat} , λ_{lon} , τ , the three components ρ_x, ρ_y, ρ_z of an impact impulse could be determined by using (13). This vector equation can be decomposed to three scalar equation including the constraints of no slip at point V_a :

$$\mathbf{u}_x^T(\mathbf{v}^+ + \boldsymbol{\omega}^+ \times \mathbf{r}_a) = 0 \quad (29)$$

$$\mathbf{u}_y^T(\mathbf{v}^+ + \boldsymbol{\omega}^+ \times \mathbf{r}_a) = 0 \quad (30)$$

as well as inelasticity

$$\mathbf{u}_z^T(\mathbf{v}^+ + \boldsymbol{\omega}^+ \times \mathbf{r}_a) = 0. \quad (31)$$

It is straightforward to show by direct calculation that $\mathbf{v}^+ + \boldsymbol{\omega}^+ \times \mathbf{r}_a$ is a linear function of $\boldsymbol{\rho}$ for fixed values of a . As a consequence, the no slip conditions and the inequality (22) determine the direction of the vector $\boldsymbol{\rho}$ (i.e. $\boldsymbol{\rho}/|\boldsymbol{\rho}|$) uniquely. At the same time, inelasticity (31) can be used to determine the length $|\boldsymbol{\rho}|$. Moreover, for slender blocks and realistic values of impact parameters, $\mathbf{u}_z^T(\mathbf{v}^+ + \boldsymbol{\omega}^+ \times \mathbf{r}_a)$ is a strictly increasing function of $|\boldsymbol{\rho}|$.

If (24) holds, then the no-slip conditions (29)-(30) associated with different values of a become equivalent. Hence, for all values of a , the direction $\boldsymbol{\rho}/|\boldsymbol{\rho}|$ of the impact impulse will be

the same. The length $|\rho|$ is however determined by (31) and it will be different for each value of a . Among these values, the largest one will provide a unique feasible solution as it implies that (31) is true, whereas for all values $i \neq a$ the inequality (23) will be satisfied instead.

In contrast, if (24) does not hold, then the no-slip conditions (29)-(30) are not equivalent, hence the direction of ρ may be different for each value of a . Thus the arguments outlined above are not applicable.

References

1. Nicholas Ambraseys and Ioannis N Psycharis. Earthquake stability of columns and statues. *Journal of Earthquake Engineering*, 15(5):685–710, 2011.
2. Aaron D Ames, Haiyang Zheng, Robert D Gregg, and Shankar Sastry. Is there life after zeno? taking executions past the breaking (zeno) point. In *2006 American control conference*, pages 6–pp. IEEE, 2006.
3. Abdolrasool Anooshehpour and James N Brune. Verification of precarious rock methodology using shake table tests of rock models. *Soil Dynamics and Earthquake Engineering*, 22:917–922, 10 2002.
4. Abdolrasool Anooshehpour, Thomas H. Heaton, Baoping Shi, and James N. Brune. Estimates of the ground accelerations at point reyes station during the 1906 san francisco earthquake. *Bulletin of the Seismological Society of America*, 89:845–853, 1999.
5. Mohammad Aslam, William G Godden, and D Theodore Scalise. Earthquake rocking response of rigid bodies. *Journal of the Structural Division*, 106:377–392, 1980.
6. Giuliano Augusti and Anna Sinopoli. Modelling the dynamics of large block structures. *Meccanica*, 27:195–211, 1992.
7. JA Bachmann, Michalis F. Vassiliou, and Božidar Stojadinović. Dynamics of rocking podium structures. *Earthquake Engineering and Structural Dynamics*, 46:2499–2517, 2017.
8. Bernard Brogliato and B Brogliato. *Nonsmooth mechanics*. Springer, 1999.
9. Nina Čeh, Gordan Jelenić, and Nenad Bićanić. Analysis of restitution in rocking of single rigid blocks. *Acta Mechanica*, 229(11):4623–4642, 2018.
10. MN Chatzis, M Garcia Espinosa, and AW Smyth. Examining the energy loss in the inverted pendulum model for rocking bodies. *Journal of Engineering Mechanics*, 143(5):04017013, 2017.
11. MN Chatzis and AW Smyth. Modeling of the 3d rocking problem. *International Journal of Non-Linear Mechanics*, 47(4):85–98, 2012.
12. MN Chatzis and AW Smyth. Three-dimensional dynamics of a rigid body with wheels on a moving base. *Journal of Engineering Mechanics*, 139(4):496–511, 2013.
13. C Christopoulos, R Tremblay, H-J Kim, and M Lacerte. Self-centering energy dissipative bracing system for the seismic resistance of structures: development and validation. *Journal of structural engineering*, 134(1):96–107, 2008.
14. Matthew J. DeJong, Laura De Lorenzis, Stuart Adams, and John A. Ochsendorf. Rocking stability of masonry arches in seismic regions. *Earthquake Spectra*, 24:847–865, 2008.
15. Angelo Di Egidio, Daniele Zulli, and Alessandro Contento. Comparison between the seismic response of 2D and 3D models of rigid blocks. *Earthquake Engineering and Engineering Vibration*, 13(1):151–162, 2014.
16. Luigi Di Sarno, Gennaro Magliulo, Danilo D’Angela, and Edoardo Cosenza. Experimental assessment of the seismic performance of hospital cabinets using shake table testing. *Earthquake Engineering & Structural Dynamics*, 48(1):103–123, 2019.
17. Vasileios Drosos and Ioannis Anastasopoulos. Shaking table testing of multidrum columns and portals. *Earthquake Engineering & Structural Dynamics*, 43(11):1703–1723, 2014.
18. Mohamed. Elgawady, Quincy Ma, John W. Butterworth, and Jason Ingham. Effects of interface material on the performance of free rocking blocks. *Earthquake Engineering and Structural Dynamics*, 40:375–392, 2011.
19. G Gazetas, I Anastasopoulos, O Adamidis, and Th Kontoroupi. Nonlinear rocking stiffness of foundations. *Soil Dynamics and Earthquake Engineering*, 47:83–91, 2013.
20. FH Hamdan. Seismic behaviour of cylindrical steel liquid storage tanks. *Journal of Constructional steel research*, 53(3):307–333, 2000.
21. GW Housner. The behavior of inverted pendulum structures during earthquakes. *Bulletin of the seismological society of America*, 53:403–417, 1963.

22. Dimitrios Kalliontzis, Sri Sritharan, and Arturo Schultz. Improved coefficient of restitution estimation for free rocking members. *Journal of Structural Engineering*, 142(12):06016002, 2016.
23. Aik-Siong Koh and Ghulani Mustafa. Free rocking of cylindrical structures. *Journal of engineering mechanics*, 116(1):35–54, 1990.
24. Dimitrios Konstantinidis and Nicos Makris. The dynamics of a rocking block in three dimensions. In *8th Hellenic Society for Theoretical and Applied Mechanics International Congress on Mechanics*, 2007.
25. Anthony N. Kounadis. On the rocking-sliding instability of rigid blocks under ground excitation: some new findings. *Soil Dynamics and Earthquake Engineering*, 75:246–258, 2015.
26. P. R. Lipscombe and S. Pellegrino. Free Rocking of Prismatic Blocks. *Journal of Engineering Mechanics*, 119(7):1387–1410, 1993.
27. L. De Lorenzis, Matthew J Dejong, and John Ochsendorf. Failure of masonry arches under impulse base motion. *Earthquake Engineering and Structural Dynamics*, 36:2119–2136, 2007.
28. MATLAB. *version 9.8.0 (R2020a)*. The MathWorks Inc., Natick, Massachusetts, 2020.
29. HP Mouzakis, IN Psycharis, DY Papastamatiou, PG Carydis, C Papantonopoulos, and C Zambas. Experimental investigation of the earthquake response of a model of a marble classical column. *Earthquake engineering & structural dynamics*, 31(9):1681–1698, 2002.
30. M. J. N. Priestley, R. J. Evison, and a. J. Carr. Seismic response of structures free to rock on their foundations. *Bulletin of the New Zealand Society for Earthquake Engineering*, 11(3):141–150, 1978.
31. F. Prieto-Castrillo. On the dynamics of rigid-block structures applications to sdof masonry collapse mechanisms, 2007.
32. Manoj Srinivasan and Andy Ruina. Rocking and rolling: a can that appears to rock might actually roll. *Physical Review E*, 78(6):066609, 2008.
33. William James Stronge. *Impact mechanics*. Cambridge university press, 2018.
34. Tamás Ther and László P. Kollár. Refinement of housner’s model on rocking blocks. *Bulletin of Earthquake Engineering*, 15:2305–2319, 2017.
35. Michalis F Vassiliou, Stefan Burger, Marius Egger, Jonas A Bachmann, Marco Broccardo, and Božidar Stojadinovic. The three-dimensional behavior of inverted pendulum cylindrical structures during earthquakes. *Earthquake Engineering & Structural Dynamics*, 46(14):2261–2280, 2017.
36. Michalis F. Vassiliou, Kevin R. Mackie, and Božidar Stojadinović. A finite element model for seismic response analysis of deformable rocking frames. *Earthquake Engineering & Structural Dynamics*, (056):1–6, 2016.
37. CE Wittich and TC Hutchinson. Rocking bodies with arbitrary interface defects: Analytical development and experimental verification. *Earthquake Engineering & Structural Dynamics*, 47(1):69–85, 2018.
38. Daniele Zulli, Alessandro Contento, and Angelo Di Egidio. 3d model of rigid block with a rectangular base subject to pulse-type excitation. *International Journal of Non-Linear Mechanics*, 47:679–687, 2012.

Figures

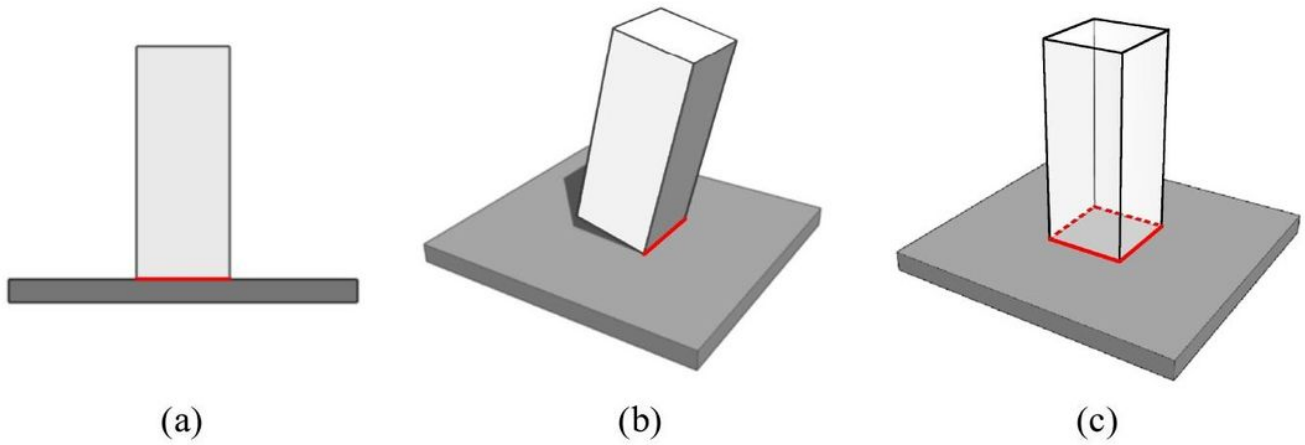


Figure 1

Three types of rocking impacts: edge impact in a planar model (a), and in a 3dimensional model (b); and facet impact in a 3D model (c).

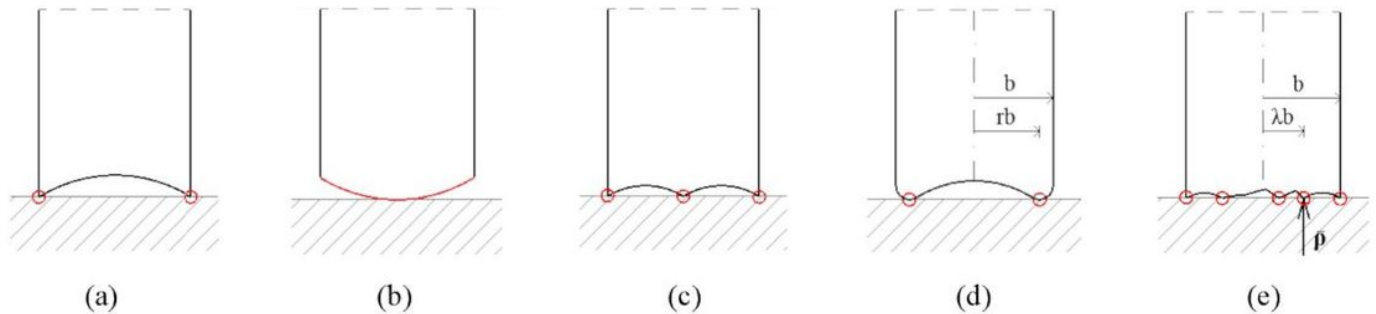


Figure 2

Illustration of geometric imperfections and their effect on a planar rocking impact. A concave edge results in the impact model of Housner (a). A slightly convex edge (b) induces no energy loss. The model proposed by Ther and Kollár (c), and by Kallitzonis (d) are consistent with other imperfections. For an arbitrary imperfection, the possible outcomes of the impact can be parametrized by a single scalar λ representing the location of the resultant ρ of the impulsive forces (e).

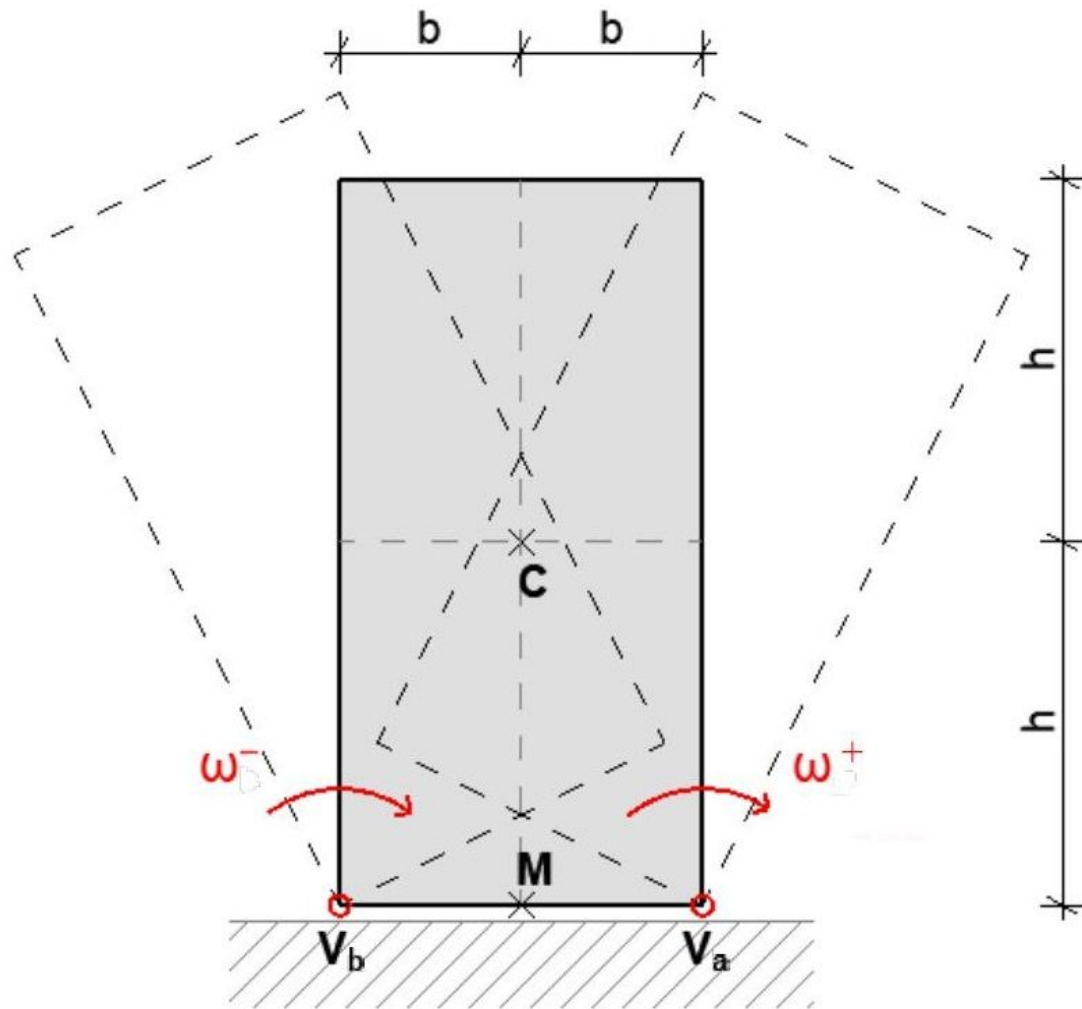
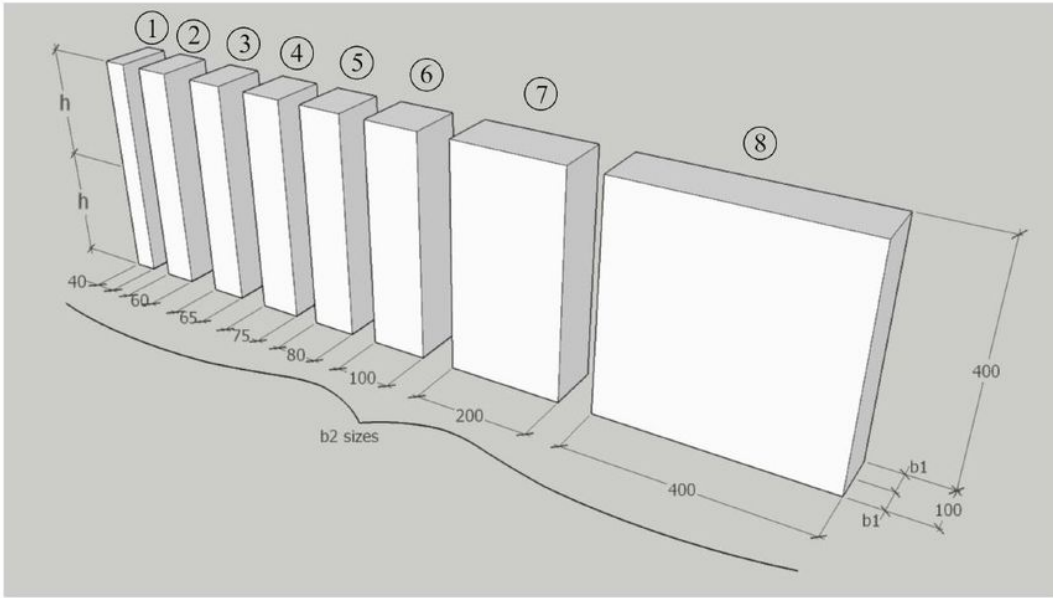


Figure 3

Rocking impact of a free-standing block in two dimensions.



(a)



(b)

Figure 4

The stone blocks used in the experiment (a), and the experimental setup with the coordinate system attached to the rocking block (b).

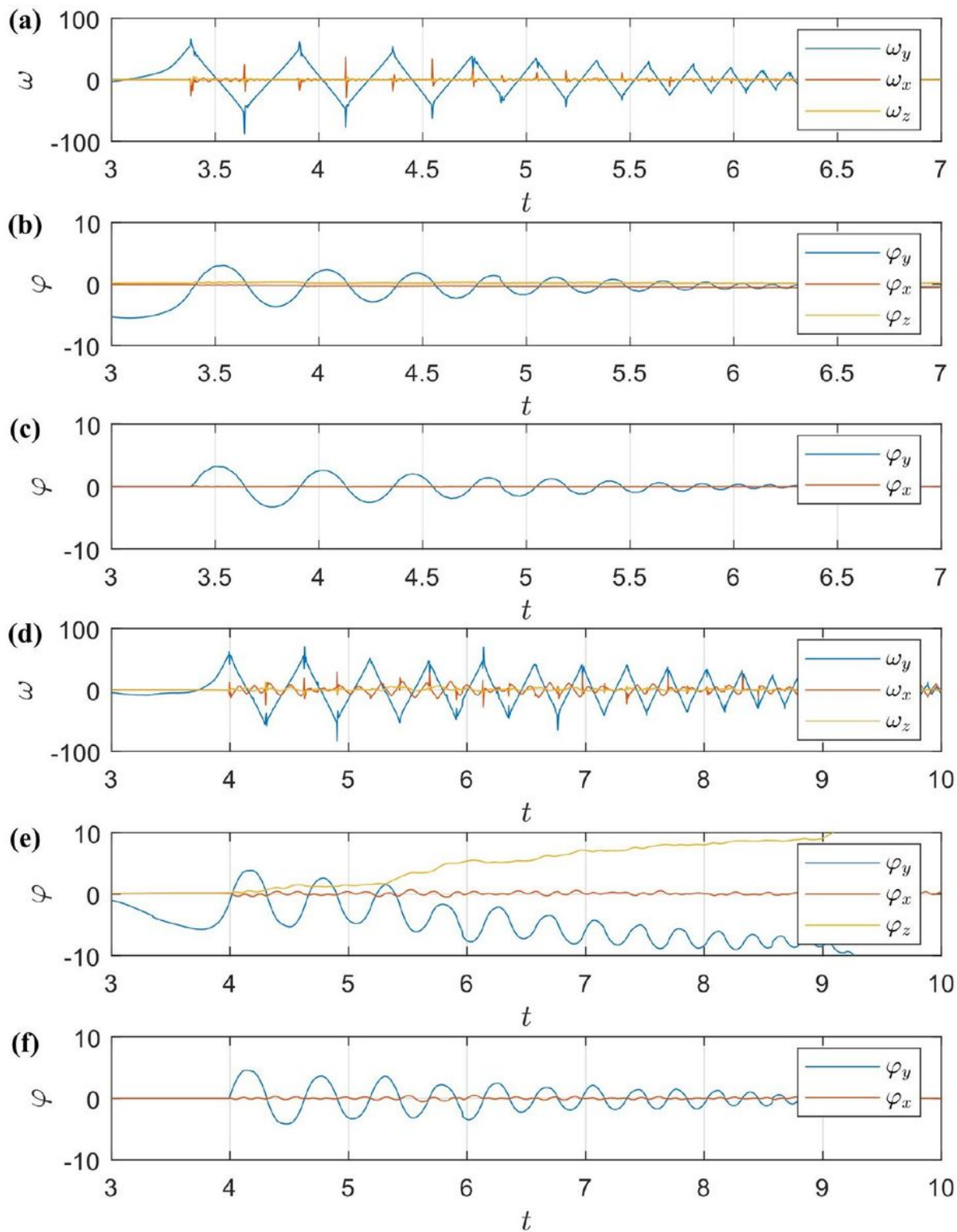


Figure 5

Measured angular velocities (a,d), Euler angles (b,e), and corrected Euler angles (c,f) of the second block rocking in positions A (a-c) and B (d-f). Note large drift in (d).

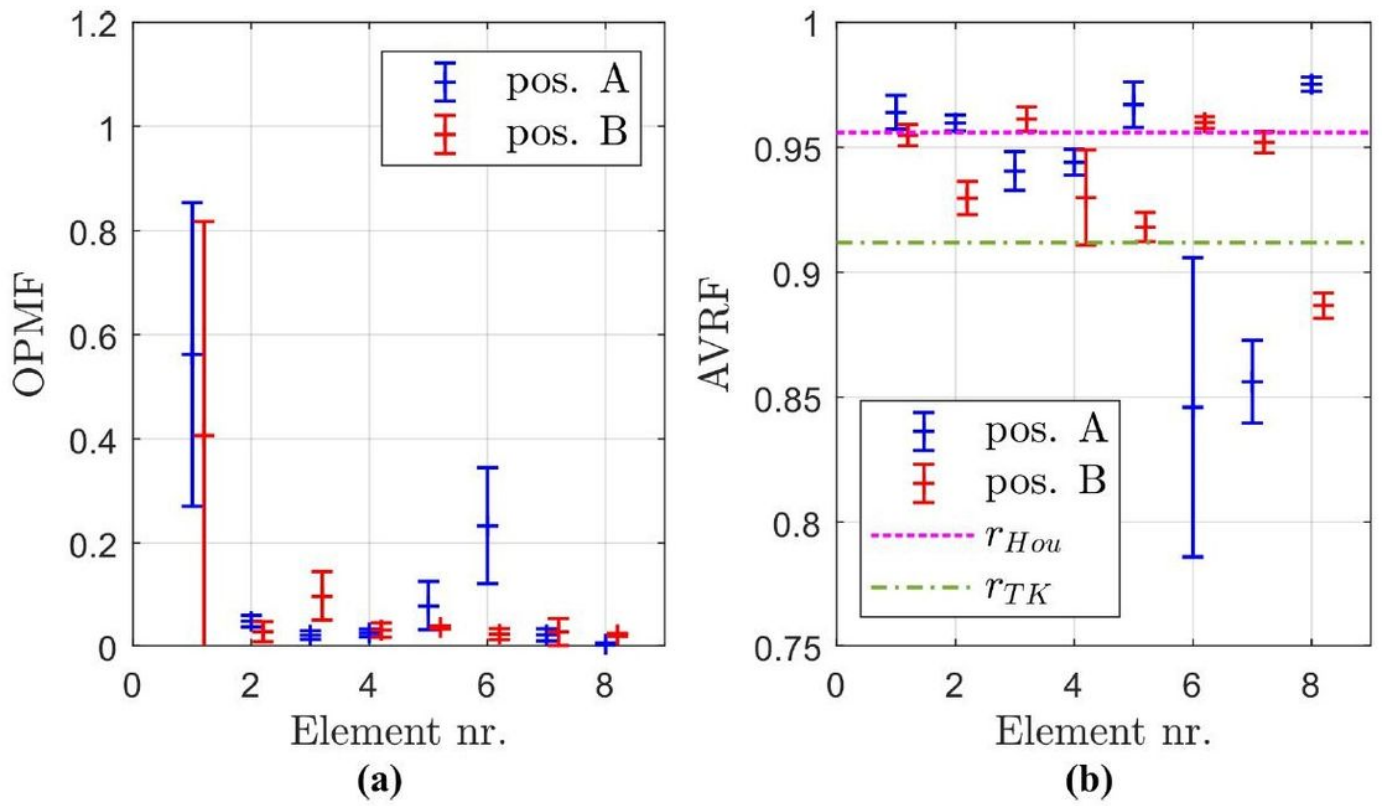


Figure 6

Mean and standard deviation of measured out-of-plane motion factors (a) and angular velocity ratios (b) for each position (A or B) of the eight blocks.

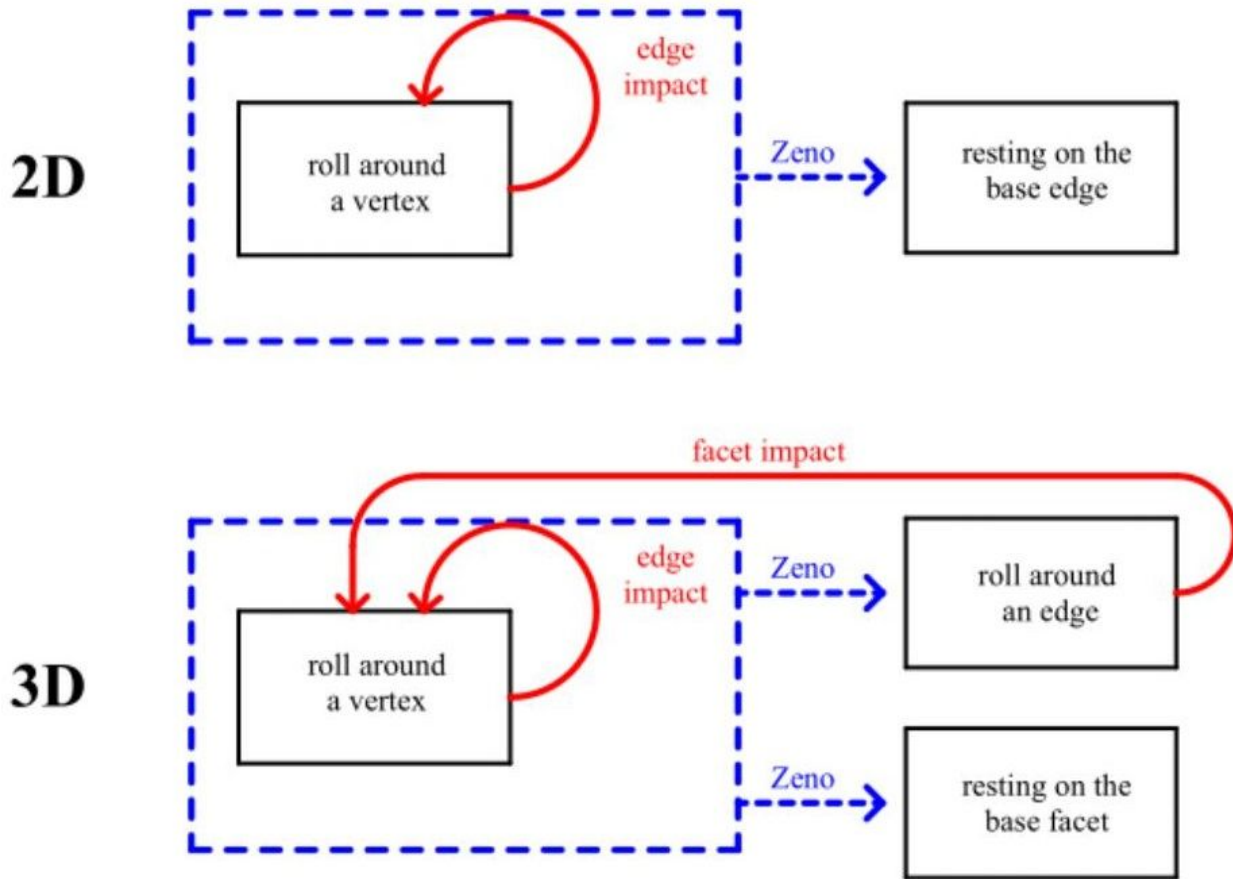


Figure 7

Transitions during two and three dimensional rocking motion.

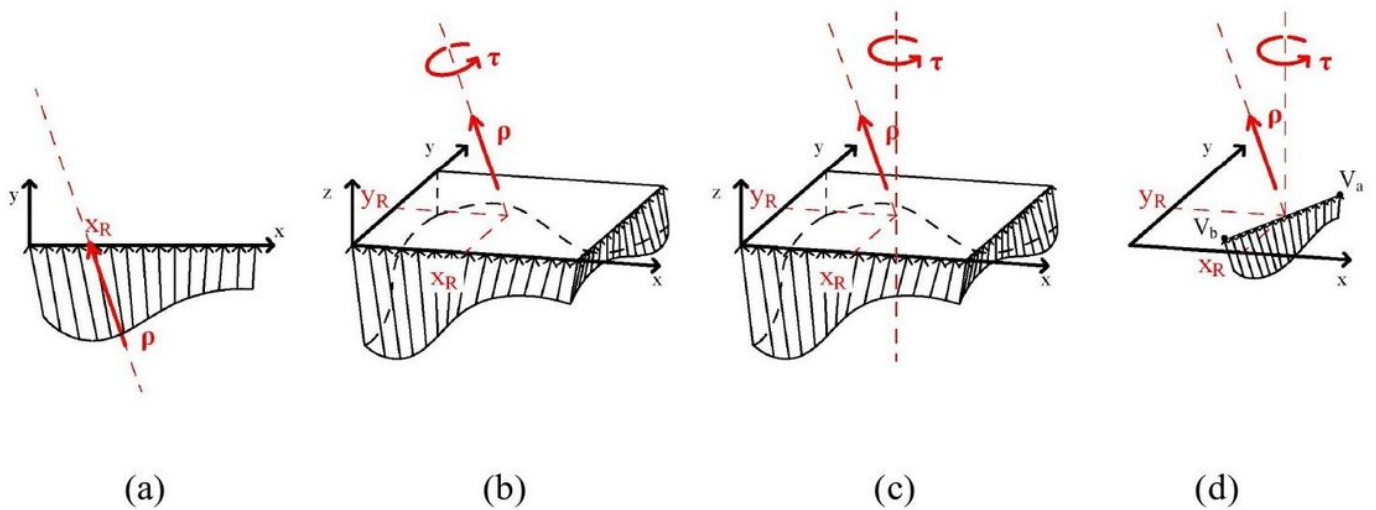


Figure 8

Resultants of distributed impulses in 2 and 3 dimensions. A planar impulse (a) distributed along a line is equivalent of a single resultant impulse ρ , which can be represented by its components ρ_x, ρ_y and its location xR . A three-dimensional impulse distributed along a surface can be represented by a resultant wrench (b) parametrized by the components ρ_x, ρ_y, ρ_z , and position xR, yR of the resultant ρ as well as by the magnitude of the torque τ . Alternatively, the same impulse can also be represented by a modified wrench consisting of a general impulse and a vertical angular momentum (c). An impulse distributed along a line section $V_b V_a$ can also be replaced by the modified wrench representation (d). In this case, the point $(xR, yR, 0)$ is a point of the section $V_b V_a$.

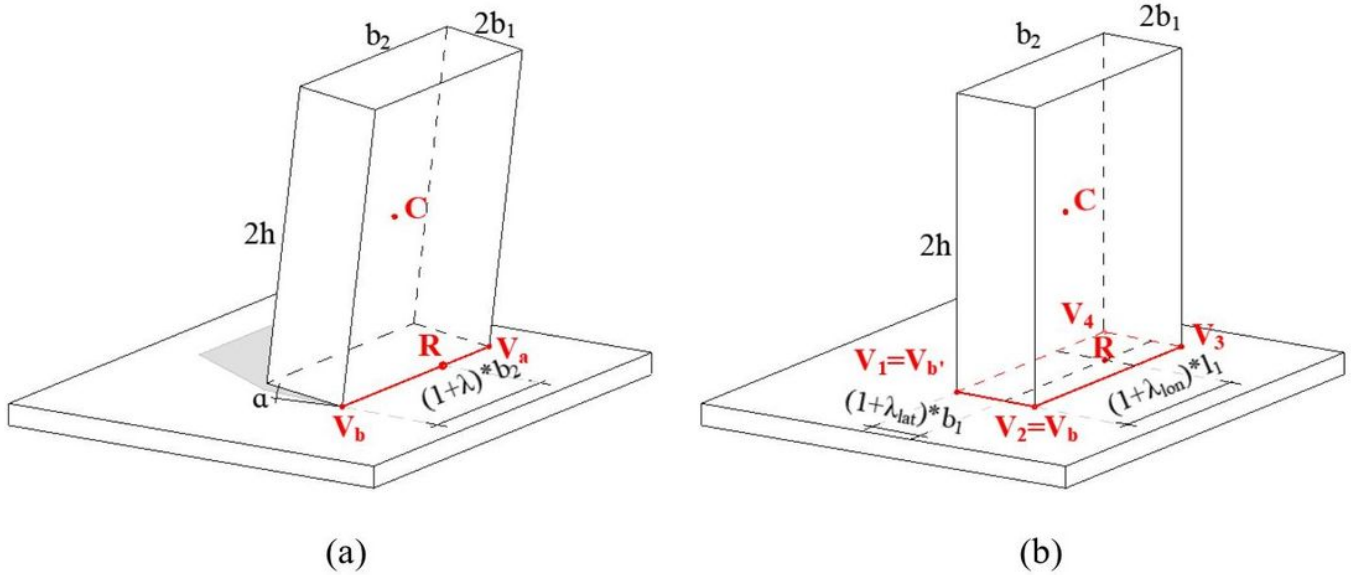


Figure 9

Notation of edge impacts (a) and facet impacts (b) illustrated by a rectangular block of size $2b_1$ by $2b_2$ by h . In (b), we assumed that the index of the V_b vertex is $b = 2$.

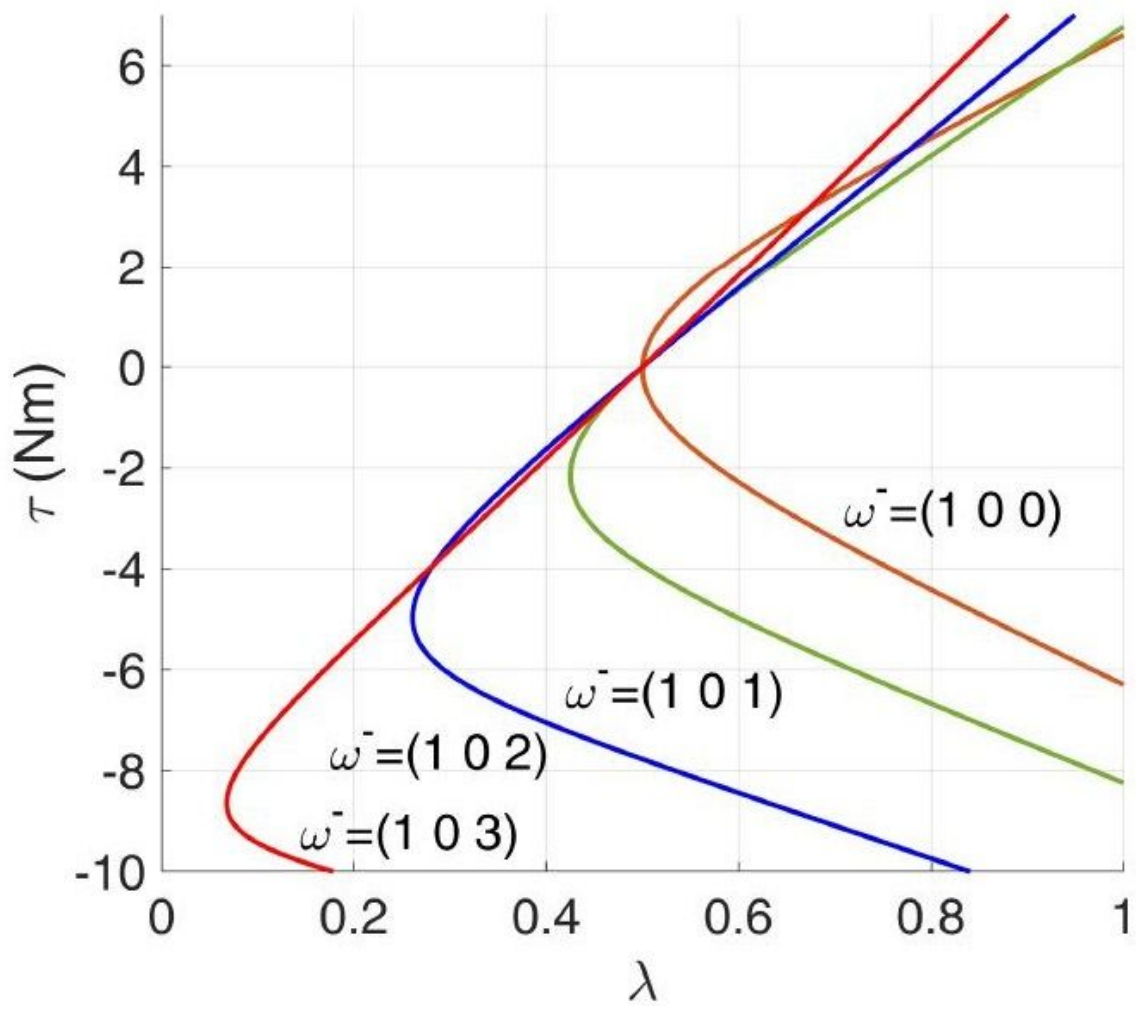


Figure 10

Energy balance of an edge impact of a homogenous block of size 10 cm by 10 cm by 40 cm and total mass 1 kg at tilt angle of 5° for several pre-impact angular velocities. The regions of the parameter plane on the right sides of the curves result in reduction of the kinetic energy. The contour lines are not affected by multiplication of ω^- by a constant factor, or by adding an arbitrary y component to ω^- .

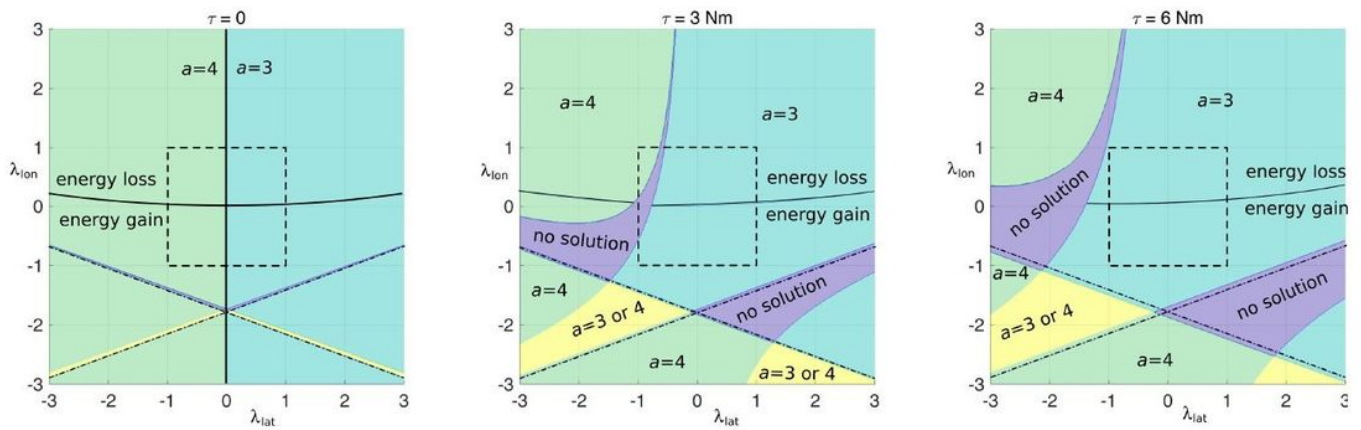


Figure 11

Theoretical bounds of a facet impact of a block with $m = 1\text{kg}$, $b_1 = 5\text{cm}$; $b_2 = 3\text{cm}$; $h = 20\text{cm}$. Pre-impact angular velocity is $\omega = [0, -1, 0]$, which corresponds to roll around edge V1V2. Each panel shows results for fixed values of τ . Background colors show the index a of the vertex in contact with the ground after the impact. Regions with no valid solution and two valid solutions also exist. Dash-dotted lines depict the singularity of (19). Dashed rectangles depict the region (27); the energy bound (26) is satisfied in the region above the continuous curves.

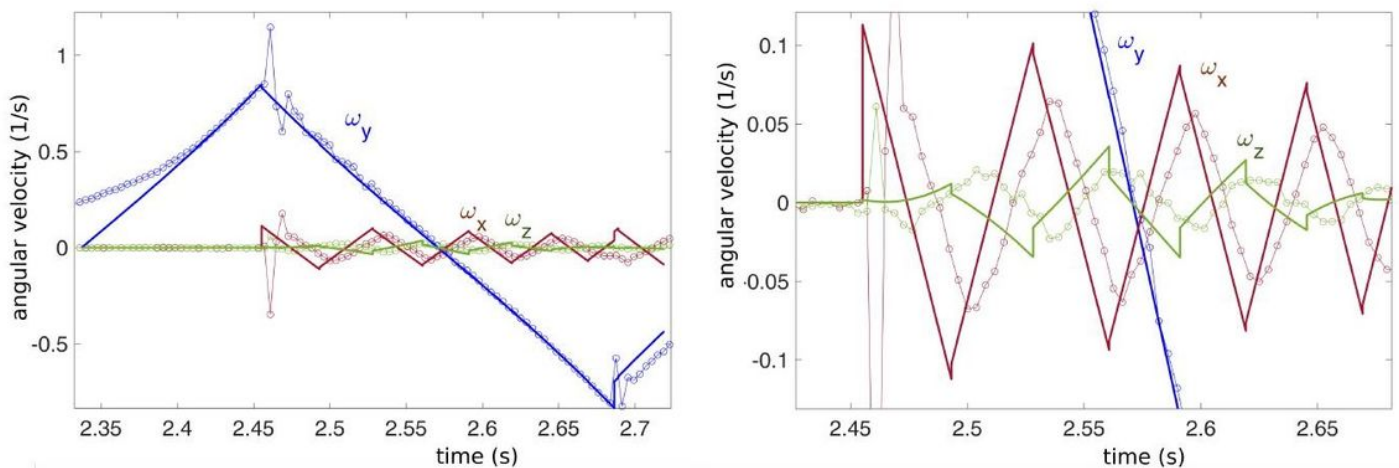


Figure 12

Left: Circles show measured angular velocities of block 4 in a free rocking test. Solid line shows simulated trajectories with optimized parameters: $t_0 = 2.33\text{s}$; $\alpha = 0.197\text{rad}$; $\lambda = 2.185$; $\lambda_{lat} = -2.032$; $\lambda_{lon} = 0.197$. Right: magnified detail of the previous diagrams. Note that each impact induces an instantaneous jump in the angular velocity, however in some cases the jump is too small to be visible.

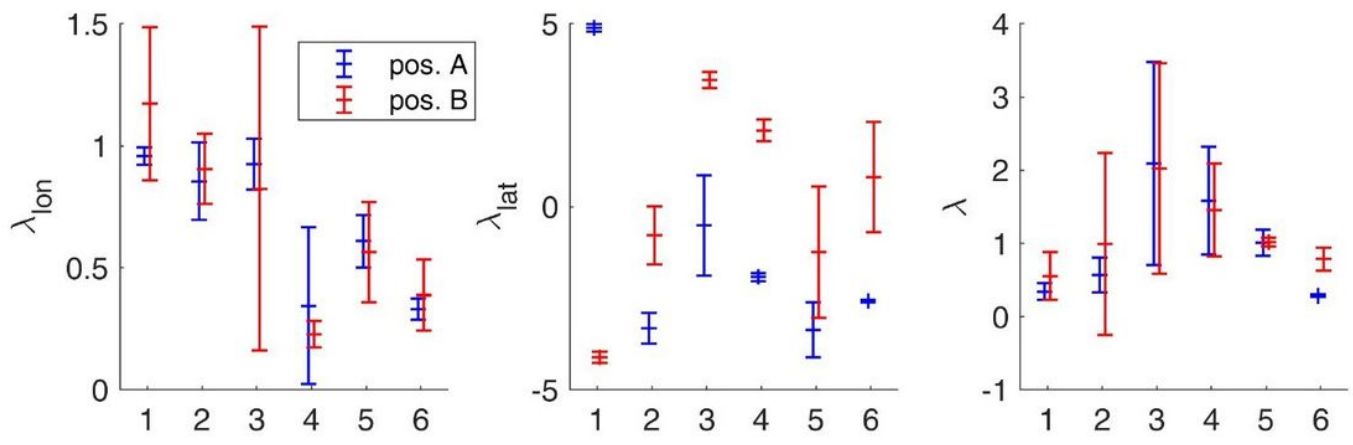


Figure 13

Numerically fitted impact parameters for the A and B positions of blocks 1 to 6.